Published in final edited form as:
IEEE Trans Med Imaging. 2005 December ; 24(12): 1529–1539.

Intrathoracic Airway Trees: Segmentation and Airway Morphology Analysis from Low-Dose CT Scans

Juerg Tschirren [Member, IEEE], **Eric A. Hoffman**, **Geoffrey McLennan**, and **Milan Sonka [Fellow, IEEE]**

J. Tschirren was with the Department of Electrical and Computer Engineering, The University of Iowa, Iowa City, IA, USA.

Eric A. Hoffman is with the University of Iowa, Dept. of Radiology, Iowa City, IA, USA.

Geoffrey McLennan is with the University of Iowa, Dept. of Internal aMedicien and Radiology, Iowa City, IA, USA.

Milan Sonka is with the Department of Electrical and Computer Engineering, The University of Iowa, Iowa City, IA, USA (email: milan-sonka@uiowa.edu).

Abstract

The segmentation of the human airway tree from volumetric computed tomography (CT) images builds an important step for many clinical applications and for physiological studies. Previously proposed algorithms suffer from one or several problems: leaking into the surrounding lung parenchyma, the need for the user to manually adjust parameters, excessive runtime. Low-dose CT scans are increasingly utilized in lung screening studies, but segmenting them with traditional airway segmentation algorithms often yields less than satisfying results.

In this paper a new airway segmentation method based on fuzzy connectivity is presented. Small adaptive regions of interest are used that follow the airway branches as they are segmented. This has several advantages. It makes it possible to detect leaks early and avoid them, the segmentation algorithm can automatically adapt to changing image parameters, and the computing time is kept within moderate values. The new method is robust in the sense that it works on various types of scans (low dose and regular dose, normal subjects and diseased subjects) *without* the need for the user to manually adjust any parameters. Comparison with a commonly used region-grow segmentation algorithm shows that the newly proposed method retrieves a significantly higher count of airway branches.

A method that conducts accurate cross-sectional airway measurements on airways is presented as an additional processing step. Measurements are conducted in the original gray-level volume. Validation on a phantom shows that sub-voxel accuracy is achieved for all airway sizes and airway orientations.

Keywords

Airway tree segmentation; pulmonary imaging; adaptive region of interest; fuzzy connectivity; quantitative analysis

I. Introduction

THE knowledge about the location of the pulmonary airway tree as well as its geometrical properties build an important step for the diagnosis, study, and treatment of lung disorders as

This work was supported in part by NIH grant HL-064368.

well as for physiological studies of pulmonary function. Low-dose CT scans are increasingly utilized in lung screening studies. Traditional region growing segmentation frequently fails due to a high noise content of low-dose images.

The work presented in this paper is divided in two parts, *airway segmentation* and *quantitative measurements*. The purpose of the airway segmentation step is to determine the location of segments of the intrathoracic airway tree from CT image volumes. The airway tree segmentation does not return precise geometrical information — an accurate delineation of the airway wall is performed by the quantitative analysis step.

Previous work on airway segmentation mainly includes region growing-based methods [1], [2], [3], [4], morphology based methods [5], [6], [7], and combinations of the two [8], [9], [10]. Other methods proposed in the past include rule based methods [11], [12], energy function minimization [7], and ROI modification-based techniques [13]. Schlathölter et al. [14] use a front-propagation algorithm for segmenting airway trees. Branchpoints are detected when the front splits up. Diameters are measured during the segmentation and a leak is identified if the diameter suddenly increases.

There are many reasons why airway tree segmentation is difficult to achieve from volumetric CT images in a robust fashion from clinical-quality or low-dose CT images. Some of the reasons are anatomy-related, e.g., airway obstructions; others are caused by heart beat induced movement artifacts and image reconstruction artifacts. Consequently, one of the biggest problems when segmenting airway trees with automated methods is leakage into the extra-luminal regions. Leaks occur because the airway-wall that separates the airway lumen from the surrounding lung parenchyma is relatively thin. The lung parenchyma, on the other hand, exhibits a texture similar to that of small airways. Partial volume effect and image noise greatly decrease the CT-visibility of the airway-wall. At some places this can cause the segmentation algorithm to “grow” through the airway-wall. Once this happens, potentially large regions of lung-parenchyma are wrongly identified as airways.

Another common problem with previously proposed airway segmentation algorithms is their difficulties with segmenting low-dose scans and scans of heavily diseased lungs, for example, lungs of emphysema patients. In the case of low-dose scans the segmentation either stops early or leaks. The user then has to run the segmentation algorithm several times in the attempt to find an optimal combination of parameters. In the case of diseased lungs, heavy leaking is not unusual.

The quantitative measurement step follows the segmentation step, and its purpose is to accurately find the location of the inner airway wall in order to conduct geometrical measurements. The medical community expresses a great interest in not only the qualitative but also the quantitative in particular also the quantitative analysis of airways [15].

In the past, measurements have often been done manually [16], [17]. Automated methods [18], [19], [20], [6], [21], [22] have been presented before. Reinhardt et al. [18], [19] showed that the accuracy of measurements depends on the size of the airway and proposed a model-based system using a 2D Gaussian function to model the point-spread function of the scanner. Prêteux et al. [20], [6] approximated the inner airway wall with a Butterworth polynomial, but concluded that their method produces a sharply increased error for small airways. Saba et al. [21] used the full-width/half-max method to conduct measurements in 2D and then model the 3D airways based on these measurements.

Our new *airway segmentation* method reported below offers fully automated and reliable identification of airway trees from CT volumes. The need for human operators to manually optimize segmentation parameters was eliminated. The algorithm works without a change on

different types of scans, e.g., low-dose and regular-dose, on diseased subjects and normal subjects while the runtime does not exceed several minutes per volume. The *quantitative airway size measurements* step provides accurate airway dimensions (minor and major diameter, cross-sectional area) on airway segments of all sizes and all possible spatial orientations (including in-plane, relative to the scanning direction). Again, the measurements are performed fully automatically, with no manual intervention.

Methods — Airway tree segmentation

A. Overview

The segmentation algorithm presented here is based on *fuzzy connectivity* as proposed by Udupa et al. [23] and Herman et al. [24].

During the execution of this algorithm, two regions – foreground and background – are competing against each other. This method has the great advantage that it can overcome image gradients and noise. The disadvantage is its relatively high computational complexity. Computing time can be reduced by splitting the segmentation space into a number of smaller subspaces and by keeping the search space as tight as possible around the airway segments.

As mentioned above, leaks into the surrounding lung parenchyma are a common problem of previously proposed airway tree segmentation algorithms. The root of a leak is a very localized phenomenon. The leak itself, the location where the segmentation result enters the lung parenchyma, normally occurs within a very small area (within a few voxels). But if the leak goes undetected then it often spreads quickly, eventually occupying substantial parts of the lung and, in many cases, rendering the airway tree segmentation useless (see Figure 1).

The desire to keep the segmentation within a small area, together with the need to detect possible leaks at their root, lead to the idea of using a relatively small adaptive region of interest (ROI) that follows the airway tree branches as they are segmented. The ROI has a cylindrical shape and adapts its geometrical dimensions, its orientation, and position to the predicted size, orientation, and position of the airway branch to be segmented. This has two main advantages:

- The segmentation process is kept close to the airway segments, therefore the individual problem size is kept small, which leads to faster segmentation time.
- Problems (leaks) can be detected early and addressed.

Figure 2 illustrates the concept. Using a cylindrically shaped ROI (versus the more common cubical ROI used in other 3D image segmentation tasks) has the advantage that the ROI better adapts to the target shape, which is close to cylindrical. This means less “useless” background voxels have to be analyzed and the computing time can be shortened. A similar approach was independently used by Mori et al. [13].

B. Multiseeded fuzzy connectivity

The basic idea of segmentation with fuzzy connectivity is that the voxels of an input image are compared with a seed-voxel and the similarity/dissimilarity is expressed as a fuzzy membership value. The similarity of two voxels c and d is expressed by the *affinity value* $\psi(c, d) = [0, 1]$, which is normally computed based on gray-values and defined for adjacent voxels only. In this application we consider 18-connected voxels as adjacent. If c and d are not directly adjacent then their similarity is compared by looking at all possible “chains” of adjacent voxels that connect c and d. The strongest chain is chosen to represent the similarity. The strength of a chain is defined by the lowest ψ value along its length (weakest link). Voxels are assigned to the foreground region if their ψ value exceeds a predefined value.

The multi-seeded fuzzy connectivity (MFC) method takes this idea one step further by growing two regions (foreground and background) simultaneously and letting them compete for voxels. The method guarantees that both resulting regions, foreground and background, are connected in themselves, i.e., no isolated "islands" may occur. The advantage of segmentation with MFC is that it can overcome image gradients and image noise without significant leaking or premature abortion of segmentation. The disadvantage of the method is that it is relatively expensive to compute, particularly for big 3Dvolumes. Methods for increasing computational efficiency are presented below.

C. Input data

To decrease the computer memory size requirements, the 12-bit gray-scale values v_{12} obtained from the CT scanner are converted into 8 bit values v_8 using the piecewise linear function

$$v_8 = \begin{cases} 0 & \text{if } v_{12} < -1000 \\ v_{12} + 1000 & \text{if } -1000 \le v_{12} \le -800 \\ \frac{55}{800} v_{12} + 255 & \text{if } -800 < v_{12} \le 0 \\ 255 & \text{if } v_{12} > 0 \end{cases} \quad (1)$$

Note that no information is lost in the range between −800 HU (Hounsfield Units) and −1000 HU, which includes all important information for the airway segmentation. This compression eases memory requirements and decreases computing time due to the decreased memory requirements.

D. Affinity functions

The airway lumen shows a mostly constant gray-level value of 0 (measured in the 8 bit volume; corresponding to −1000 HU) throughout the whole airway tree. Exceptions are noise voxels, frequently seen in low-dose scans. An affinity function based on the absolute value of the gray-value can be used. The affinity μ_{fg} of a foreground voxel v is solely based on the gray-value i of v and is defined by

$$\mu_{fg}(i) = e^{-\frac{(i-\mu_0)^2}{2\sigma^2}} \quad (2)$$

In the presented methods, values of $\mu_0 = 0$ and $\sigma = 100$ were determined experimentally and were kept constant across all analyses. The exact values turned out to be not very critical — the segmentation result is nearly identical over a relatively wide range of μ_0 and σ.

The average gray-value of the airway wall changes substantially between different airway generations. For the first generation (trachea), the gray-values of the wall voxels are mostly in the range of 0 to −200 HU. But further down the tree, at the 5th or 6th generation, for example, the gray-values are in the range of −300 to −800 HU. This shift is caused by the partial volume effect introduced by the X-ray beam collimation and the sampling process in the CT scanner to which the thinner airway walls of the higher-generation airways are more sensitive. Motion artifacts and/or anatomical obstructions further complicate the problem.

Because of the gray-value gradient, the affinity function μ_{bg} for the airway wall is based on the gray-value difference between two voxels v_1 and v_2 and is defined by

$$\mu_{\mathrm{bg}}(i_1, i_2) = \begin{cases} \mu'_{\mathrm{bg}}(i_1, i_2) & \text{, if } v_1 \text{ and } v_2 \text{ are 18-connected} \\ 0 & \text{, otherwise} \end{cases} \quad (3)$$

with i_1 and i_2 being the gray-values of v_1 and v_2, respectively,

$$\mu'_{\mathrm{bg}}(i_1, i_2) = \exp\left(- \frac{\left[(i_1 - i_2) / 2 - \mu_0 \right]^2}{2\sigma^2} \right) \quad (4)$$

and Note that the background corresponds to the airway wall and that the parenchymal parts of the lung volume are not utilized in the MFC segmentation.

E. Directional affinity

With the affinity functions described above, some leaks are unavoidable due to voxel-connections at the -1000 HU level between airway lumen and lung parenchyma. Such leaks are mostly a very localized phenomena; the "leaking bridge" is normally only one or two voxels wide. Adding *directional information* to the affinity function helps prevent them.

Directional affinity uses information about the expected spatial direction of the current airway segment. Figure 3-a illustrates the concept in 2D. When computing the affinity value between a voxel c and its neighbors n, only neighboring voxels that lie close to the axis of the expected direction D are considered, i.e., voxels $n_{0,0}$, $n_{1,0}$, and $n_{2,0}$ in Figure 3b. All other neighbors get an affinity value of zero assigned, relative to c. Additionally, the affinity value also depends on the gray values of further neighbors in direction D. The directional foreground affinity $\mu_{\mathrm{fg}}^{\mathrm{dir}}(c, n_{i,0})$ is computed with

$$\mu_{\mathrm{fg}}^{\mathrm{dir}}(c, n_{i,0}) = \min_{j=0\ldots2} \left[\mu_{\mathrm{fg}}(c, n_{i,j}) \right] \quad (5)$$

The direction D is given by the spatial orientation of the ROI. 26 discrete directions are possible as illustrated in Figure 3b. With a given ROI the closest discrete direction is used.

Figure 4 shows an example where a leak was successfully avoided with the help of directional affinity.

F. Positioning new cylindrical regions of interest

The surface of the segmentation result in Figure 5(a) is found by a queue-based region-grow algorithm that only grows along foreground-voxels that are in the 6-connected neighborhood of at least one background-voxel. Additionally, the algorithm distinguishes between surface voxels that are situated below the surface of the ROI-cylinder, and voxels that lie on the surface of the ROI. We call an isolated (8-connected) group of the latter a *surface face*. Surface faces are used for initializing the skeletonization process. The orientation of new ROIs is determined based on the skeleton of the current segmentation result. A rough skeletonization suffices for that purpose; exact branch-point positions and smoothed skeletal lines are not important. A computationally efficient skeletonization is implemented by first computing the distance map of the segmentation result. A simple graph search is then executed using the centers of gravity of the surface faces as anchor points. If there are more than two surface faces found along the surface of the ROI then at least one branch-point must have been encountered.

The exact location of an ROI is not critical. The length of an ROI may for example be expanded such that it partially covers a neighbor airway branch. In that case the neighbor branch will

still be explored independently since it was already detected during the evaluation of the parent-ROI.

An ROI may end in the middle of a branch-point. This case is detected by an unusual increase in the area of the face at the "downstream" end of the ROI. In that case the length of the ROI is increased and the segmentation is repeated. This makes sure the roots of the child-branches are detected correctly. The default length of an ROI is 25 voxels and it can be lengthened at most twice (by a factor of 2 each time).

G. Seedpoints

Two seedpoints are needed for the segmentation of each ROI: one within the airway lumen and one within the airway wall. For the initial ROI an additional seedpoint is required to determine the spatial orientation of the ROI. These initial three seedpoints are automatically found by searching for the trachea. In the transversal view the trachea is a roughly circular object that is located approximately in the center in the field of view. Further more the cross-sectional area is within a known range. Taking this pre-knowledge the CT volume is thresholded slice by slice and a circular object is sought that fits the description above. If such an object can be found continuously over several consecutive slices then the trachea is found. This identifies the lumen- and the orientation-seedpoints. The wall-seedpoint is identified by seeking the immediate periphery of the lumen for a bright voxel.

The two seedpoints for every consecutive ROI are found similarly. The lumen seedpoint is identified as the first center-line voxel that lies within the new ROI, and the wall-seedpoint is again found by scanning the lumen's periphery for a bright voxel.

H. Leak detection

By closer examination of typical leaks, it was observed that a leaked segmentation result almost always exhibits a "spongy" structure – it contains many holes and tunnels. A leak-free segmentation result, on the other hand, almost never shows these properties. This observation was used to build a leak detector. A sequential- and topology-preserving thinning [25] is applied to the segmentation result. The size of the resulting *topological kernel* is used as a leak detector. The topological kernel is the object that remains after the sequential thinning step removed all voxels that can be deleted without altering the topology of the object. A topological kernel of size 1 (one single voxel) is an indicator for a solid segmentation result (→ no leak). A topological kernel of size > 1 indicates that a leak occurred. In other words, if for example the segmentation result contains a hole then the thinning result (the topological kernel) will have the shape of a ring. Naturally this ring must consist of more than one voxel and this is taken as an indication of a leak.

I. Framework

Within the algorithm, the term *frame* refers to the data structure that contains all the information needed for segmenting one ROI position. This includes the information about the position, orientation, and size of the ROI itself, the parameters for the foreground and background affinity functions, the position of the seed points, the topological generation number of the current airway segment, and information about the current status and the number of previously failed segmentation attempts at this position.

Frames that are to be processed are put into a *priority queue*, which uses the generation number of the airway segment as the sort key. The dequeue function of the priority queue always returns the frame with the lowest generation number available in the queue. The result is that the tree grows evenly. The segmentation of lower generation segments is finished before the segmentation of any higher generation segments is attempted. An advantage of this concept is

that the number of segmented airway generations can be controlled, which saves computing time if only a few generations are to be retrieved.

If a segmentation problem (e.g., leak) is detected then the segmentation result of the last frame is deleted, the parameters of the affected frame are modified, and the frame is re-queued. Possibly modified parameters include the geometry of the ROI (diameter, length, and position) and the affinity function (values for μ, σ, and directionality). The kind of parameter changes depends on the type of segmentation problem and is controlled by a pre-defined finite state machine. This finite state machine has a depth of 3, i.e., if the segmentation of a particular frame still fails after 3 parameter changes then this frame is given up permanently and segmentation continues at a different airway branch.

III. Methods — Quantitative analysis

The process of quantitative analysis of airway segments uses the results of the previously-described segmentation of the airway tree (Section II). Consequently, approximate surfaces of the airway tree segments together with the airway tree skeleton centerlines are used to guide the accurate detection of the airway walls. The process is thus divided into three steps (Figure 6):

- Re-sample 2D slices perpendicular to airway segments.
- For each 2D slice separately, segment airway wall.
- Conduct measurements on segmentation result.

A 2D slice I_{gray} is re-sampled from the original gray-level volume using the centerline information, and a 2D slice I_{seg} is re-sampled from the earlier airway segmentation result. The slices are oriented perpendicular to the centerline of the respective airway segment and one pair of slices is re-sampled for every centerline voxel position. Re-sampling at every centerline voxel position assures that every possible position along the airway tree segments is covered by measurements. The perpendicular orientation is determined by computing the tangent to the smoothed centerline (the centerline is obtained from the skeletonization process). Re-sampling is performed using tri-linear interpolation.

For every voxel along the centerline, the wall-segmentation takes I_{gray} and I_{seg} as input and outputs $\vec{P} = \left[\vec{p}_0, \vec{p}_1, \ldots \vec{p}_{N-1}\right]$ with $\vec{p}_i = \left(x_i, y_i\right)$ as output, where $\vec{p}_{0\ldots N-1}$ represent the segmented points along the inner airway border, defined in the Cartesian coordinate system of I_{gray} *Dynamic programming* [26] is used for the wall-segmentation. The input images are *radially re-sampled* in order to "stretch" the target border. Starting from the point defined by the centroid of the segmentation result in I_{seg}, a total of $N = 800$ evenly spaced rays are cast, and along each ray $M = 130$ points are sampled from I_{gray} and I_{seg}. This results in the images I^{rad}_{gray} and I^{rad}_{gray} of dimension M × N shown in Figure 7 c) and a).

The cross-sections of airways are normally not perfectly circular, and as a result the airway-wall borders in Figures 7 a) and c) are not completely straight after resampling. The straightness of the border is however preferred for the graph search-based segmentation so that the preliminary airway segmentation can be used for guidance. Therefore, a local *horizontal shift* is applied to the radially re-sampled segmentation result shown in Figure 7 a) so that the straightened image results – Figure 7 b) (the transform is such that the transition between black and white is positioned in the center of the image). Simultaneously the same horizontal shift is applied to the corresponding line in the radially re-sampled gray-image – Figs. 7 c,d). The amount and direction of shift as well as the radial position of every re-sampled point are

recorded so that at the end of the segmentation process the resulting border points can be mapped back into the original 2D slices.

The *cost-function* I_{cost} used for the dynamic programming uses the first and second derivatives of the gray-level image and is based on a cost function proposed in [27]. Strictly speaking the cost-function used here should be called the "reward"-function since higher values are preferred over lower ones. But to be consistent with the literature the more common term *cost-function* is used here – and the dynamic programming is maximizing the cost

$$\mathcal{I}_{\text{cost}} = \omega \cdot \underbrace{\mathcal{I}_{\text{smooth}} \star \mathcal{M}_{\text{Sobel}}}_{\text{first derivative}} \dot{+} (1-\omega) \cdot \underbrace{\mathcal{I}_{\text{smooth}} \star \mathcal{M}_{\text{Marr}}}_{\text{second derivative}} \quad (6)$$

where ★ symbolizes a 2D convolution, the $\dot{+}$ symbol stands for point-wise summation, I_{smooth} is I^{rad}_{gray} smoothed with a 5 × 5 unit matrix. M_{Sobel} is a 5 × 5 Sobel mask, and M_{Marr} is a 5 × 5 Marr mask. By changing the value of constant ω, the position of the resulting border can be pushed or pulled radially as illustrated in Figure 8. This is based on a wellknown behavior of 1st- and 2nd-derivative edge detectors that consistently position their maximum edge responses on one or the other side of the true edge, respectively. Consequently, weighting their responses can be used for accurate positioning of the edge detection response with respect to the correct edge location. The purpose of this is to adapt the cost-function to the estimated size of the current airway segment and thus maintain a high degree of measurement accuracy across all sizes of airways. The size of the airway is estimated based on a pixel-count in the re-sampled segmentation result I_{seg}. The value of ω is determined via the empirically determined piece-wise linear function shown in Figure 9. The values of ω were found by an optimization process during which phantom CT images of tubes with known sizes were used, the sizes covered the full range of airway sizes and corresponded to the CT imaging parameters used for the in vivo scans.

Measurements are conducted on the segmented border $\vec{P}$, where $\vec{P}$ represents a polygon. The cross-sectional area is computed and the minor (minimal) and major (maximal)diameters are found. The minor and major diameter lines are guaranteed to pass through the center of gravity of the area inscribed by $\vec{P}$. The results are written into an XML file that holds all tree-related data (topology, geometry, anatomical labels, measurements) and allows easy access to data for further processing.

IV. Validation of airway segmentation

A. Method

Validation of the airway segmentation would ideally be based on a gold standard provided by a human expert who would perform hand-tracings of all discernible airway segments for several airway trees. Unfortunately this approach is not feasible due to the extreme labor-intensity of the hand-tracing task.

Alternatively, a validation scheme was developed that is based on anatomical labeling and compares the segmentation result of the newly proposed algorithm with the result of a region growing-based segmentation algorithm that was previously published and that was specifically developed for airway tree segmentation [28]. Low-dose CT scans (120 kV, 50 mAs, voxel size $0.68 \times 0.68 \times 0.6\ mm^3$) from 22 different patients were used, and a human expert assigned as many anatomical labels as possible to every segmentation result. A total of 32 unique anatomical labels (Figure 11) are commonly used in human airway trees and the same level of

labeling was attempted for the reported validation. The 32 labels represent an international standard used for anatomical labeling of airways for bronchoscopic and other purposes [29]. For every CT scan the two segmentation algorithms were compared based on the number of discerned airway segments.

The newly proposed algorithm was run only once on every CT dataset, using the same parameter settings for all datasets. The region-grow algorithm was run 12 times on every dataset, using different combinations of user-adjustable input parameters. The best region-grow result was hand-selected (by visually inspecting all segmentation results and choosing the one result with the highest number of branches and no significant leaks). This best region-grow result was then used for the anatomical labeling.

Figure 12 shows a typical comparison of two segmentation results.

B. Results

Table I lists the count of named segments that were segmented by two segmentation methods.

On average the newly proposed segmentation method identified 27.0±4.4 anatomically named segments per tree (mean ± standard deviation), while the region-grow algorithm returned 21.3 ± 8.7 named segments. The new method statistically significantly outperformed the region growing method ($p = 0.011$). Across all tested trees there was a total of 132 anatomically named segments that were segmented by the new method, but missed by the region-grow algorithm. On the otherhand, there was only a total of 3 named segments that have exclusively been segmented by the region-grow method. In the most extreme single CT dataset, the new method found 23 named segments more than the region-grow method. In contrast to that, the region-grow algorithm never identified more than one extra named segment per tree in comparison with the new method.

Figure 14 shows the average count of anatomically named segments as a function of the generation number.

V. Validation of the cross-sectional measurements

A. Method

The validation of the quantitative analysis method would ideally be based on in-vivo scans. The problem with this approach is that no accurate, reliable, and independent reference measurements are available (accuracy at voxel or sub-voxel level, i.e., 0.6 mm). Therefore a physical phantom made of Plexiglas tubes was used for the validation of the quantitative analysis. The phantom contains 7 tubes of known diameters in the range between 0.98–19.25 mm. Since the lumen of the smallest tube was invisible on the CT scans, the smallest tube was excluded and the analysis was based on the remaining 6 tubes. The space between the individual tubes was filled up with dried potato-flakes, which closely resemble the texture of lung parenchyma when scanned with a CT scanner. The phantom was scanned in 4 different angles of 0°, 5°, 30°, and 90°, rotated in the coronal plane. Three different scan settings were used [*low dose* (120 kV, 50 mAs), *regular dose* (120 kV, 100 mAs), *high dose* (120 kV, 200 mAs)], all at a voxel size of $0.39 \times 0.39 \times 0.6$ mm^3.

B. Results

Tables II–IV summarize the results from the measurements on the Plexiglas phantom. The difference between nominal diameter d_{nom} and the average measured diameter d_{μ} is listed for all combinations of tube size and scan angle φ. Mean μ and standard deviation σ values are

given for all scan angles at a given tube size (bottom two rows), as well as for all tube sizes at a given scan angle (two rightmost columns).

It can be seen that the average absolute deviation from the nominal diameter never exceeded 0.26 millimeters. The single largest deviation was measured to be −0.46 millimeters (Tube nr. 5 with a nominal inner diameter d_{nom} of 9.50 mm, scanned at $\varphi = 90°$, regular dose). Comparing this with the voxel size of $0.391 \times 0.391 \times 0.6\ \text{mm}^3$ shows that the method works at sub-voxel accuracy. This is possible because the gray-image is re-sampled before the border is detected (see Section III).

VI. DISCUSSION

Compared with region growing-based airway tree segmentation, the newly proposed *segmentation algorithm* not only identifies more airway segments (higher mean number of retrieved segments), but it does so more consistently (smaller standard deviation). This difference becomes especially apparent with trees like the one depicted in Figure 10, where the new method returns a markedly better result. From Figure 14 it can be seen that the new segmentation method always returns all segments of the first 3 generations (zero standard deviation), whereas the region-grow method misses branches of generation-numbers as low as 2 (main bronchi) in some cases. It is also notable that the new algorithm achieves this result without the need for the user to hand-optimize parameters. In contrast, the parameters for the region-grow algorithm were hand-optimized to get the best possible result.

The segmentation result is mostly unaffected by the choice of the initial seedpoint. In some cases minor leaks into the surrounding lung parenchyma may occur. This is the case if a leak is “solid”, i.e., it does not have any holes and consequently it is not recognized as a leak. However this happens relatively rarely, and if it does then such a leak is normally restricted to a relatively small area. We never observed high-volume leaks such as the ones often seen in regiongrow-based segmentation results.

The segmentation method is sensitive to motion artifacts such as heart beat induced bronchus movement, as well as airway obstructions caused for example by mucus. If one of these artifacts causes an airway-lumen to be completely obstructed then the segmentation of the affected airway branch will not be continued at this point (the same happens in regiongrow based algorithms). It is mostly small airways (at the sub-lobar level) that are affected by this. We plan to address this problem in our future work.

The *quantitative analysis* achieves sub-voxel accuracy on average. Only a very few isolated measurements show a deviation of around 1 voxel from the nominal value.

It is interesting to note that no considerable difference in the average accuracy can be observed between measurements on airways that run perpendicular to the scan-plane (phantom at $\varphi = 0°$), and airways that run in-plane (phantom at $\varphi = 90°$). Other methods for the quantitative analysis of airways — namely those that conduct measurements on the 2D scan-plane only — show difficulties measuring in-plane or close to in-plane airways.

A scan of a Plexiglas-and-potato-flakes phantom is, of course, not an ideal substitute for a scan of an in-vivo human lung. It would certainly be desirable to do a similar validation on in-vivo data. Unfortunately, no precise reference measurements (with an accuracy of ½ mm or better) are available for in-vivo data. The phantom used here is the best currently available reference.

VII. CONCLUSION

A *segmentation algorithm* has been developed that works fully in 3D. It is able to detect leaks and prevent them as they occur. The developed application is user-friendly — there are no parameters that have to be tuned at runtime. The algorithm was tested on a total of 22 low-dose scans. The new segmentation algorithm proves to be considerably more robust than regiongrow-based airway segmentation algorithms, since parameters that have to be tuned by the user have been completely eliminated. In many cases the new algorithm outperforms region growing-based segmentation methods. For many of the scans regiongrow-based methods provide usable results only after several runs of the algorithm and considerable tuning of parameters. The new airway-segmentation algorithm presented here delivers good or very good results in all cases, after only one single run of the algorithm per tree. In 2 out of the tested 22 cases the new algorithm returned a somewhat inferior result when compared to the regiongrow based algorithm. In these 2 trees, high generation airway segments were missing, although the resulting trees were generally still of a good quality. A total failure of the new algorithm, for example , with severe leaks or missing lobes or sub-lobes, was *not* observed in any of the test cases.

The runtime of the newly proposed algorithm is kept down to about 3 to 10 minutes (measured on a 1.2 GHz AMD Athlon™ system) and depends on the size of the tree and the image quality. Segmentation time was measured on a single-CPU system. The segmentation algorithm is highly parallelizable. Utilizing both CPUs of a symmetric multi processor (SMP) system is expected to cut the segmentation time down to almost half.

The proposed method for the *quantitative analysis* of airway-tree segments works fully in 3D and performs the measurements in the original gray-scale volume for increased accuracy. Information from anatomical labeling is used, which makes it possible to perform measurements on specific anatomical segments named by the user. The algorithm was verified on a series of high-resolution scans taken from a physical phantom. The phantom contains Plexiglas tubes with known diameters ranging from 1.98 mm to 19.25 mm. The validation showed that the proposed method delivers sub-voxel accuracy for *all* scan-directions (including in-plane airways).

The analysis of a complete airway tree scanned at the total lung capacity takes about 3 minutes ± 30 seconds (measured on a 1.2 GHz AMD Athlon™ system), depending on the size of the tree. This includes the measurement of all anatomically named segments; measurements are taken at every centerline point along the full length of the segments.

ACKNOWLEDGMENTS

The authors would like to thank Martin Urschler, Technical University Graz, Austria, for developing the software tool that allowed the hand-labeling of the segmentation results.

REFERENCES

1. Chiplunkar, R.; Reinhardt, JM.; Hoffman, EA. Segmentation and quantitation of the primary human airway tree. SPIE Medical Imaging; San Diego, CA: 1997.
2. Tozaki T, Kawata Y, Niki N, Ohmatsu H, Kakinuma R, Eguchi K, Kaneko M, Moriyama N. Pulmonary Organs Analysis for Differential Diagnosis Based on Thoracic Thin-section CT Images. Nuclear Science, IEEE Transactions on 1998;45:3075–3082.
3. Mori K, Suenaga Y, Toriwaki J. Automated anatomical labeling of the bronchial branch and its application to the virtual bronchoscopy. Medical Imaging, IEEE Transactions on 2000;19:103–114.
4. Law, TY.; Heng, PA. Automated extraction of bronchus from 3D CT images of lung based on genetic algorithm and 3D region growing; SPIE Proceedings on Medical Imaging, San Diego, CA; 2000. p. 906-916.

5. Pisupati, C.; Wolf, L.; Mitzner, W.; Zerhouni, E. Mathematical morphology and its applications to image and signal processing. Kluwer Academic Publishers; 1996. Segmentation of 3D pulmonary trees using mathematical morphology; p. 409-416.
6. Prêteux F, Fetita CI, Grenier P, Capderou A. Modeling, segmentation, and caliber estimation of bronchi in high-resolution computerized tomography. Journal of Electronic Imaging 1999;8:36–45.
7. Fetita, CI.; Prêteux, F. Quantitative 3D CT bronchography; Proceedings IEEE International Symposium on Biomedical Imaging (ISBI'02), Washington DC; 2002.
8. Bilgen, D. The University of Iowa, IA; USA: 2000. Segmentation and analysis of the human airway tree from 3D X-ray CT images. Master's thesis
9. Kiraly, AP. The Pennsylvania State University, Dept. of Computer Science and Engineering; 2003. 3D Image Analysis and Visualization of Tubular Structures. Ph.D. dissertation
10. Aykac D, Hoffman EA, McLennan G, Reinhardt JM. Segmentation and analysis of the human airway tree from 3D X-Ray CT images. IEEE Trans. Medical Imaging. 2003
11. Sonka, M.; Sundaramoorthy, G.; Hoffman, EA. Physiology and Function from Multidimensional Images. 2168. 1994. Knowledge-Based Segmentation of Intrathoracic Airways from Multidimensional High Resolution CT Images. Proceedings SPIE
12. Park W, Hoffman EA, Sonka M. Segmentation of intrathoracic airway trees: a fuzzy logic approach. Medical Imaging, IEEE Transactions on 1998;17:489–497.
13. Kitasaka, T.; Mori, K.; Hasegawa, H.-i.; Suenaga, Y.; Toriwaki, J.-i. Extraction of bronchus regions from 3D chest X-ray CT images by using structural features of bronchus; Computer Assisted Radiology and Surgery (CARS) 2003, International Congress Series 1256, Elsevier, 2003; 2003. p. 240-245.
14. Schlathölter, T.; Lorenz, C.; Carlsen, IC.; Renisch, S.; Deschamps, T. SPIE Medical Imaging 2002. Image Processing. San Diego, CA; 2002. Simultaneous Segmentation and Tree Reconstruction of the Airways for Virtual Bronchoscopy; p. 103-113.
15. King GG, Müller NL, Parè PD. Evaluation of Airways in Obstructive Pulmonary Disease Using High-Resolution Computed Tomography. Am. J. Respir. Crit. Care Med 1999;159:992–1004. [PubMed: 10051284]
16. King GG, Müller NL, Whittall KP, Xiang Q-S, Parè PD. An Analysis Algorithm for Measuring Airway Lumen and Wall Areas from High-Resolution Computed Tomographic Data. American Journal of Respiratory and Critical Care Medicine 2000;161:574–580. [PubMed: 10673202]
17. Wood, SA.; Zerhouni, EA.; Hoford, JD.; Hoffman, EA.; Mitzner, W. Quantitative 3-D reconstruction of airway and pulmonary vascular trees using HRCT; SPIE Proceedings Biomedical Image Processing and Biomedical Visualization. San Jose, CA; 1993. p. 316-323.
18. Reinhardt JM, D'Souza ND, Hoffman EA. Accurate Measurement of Intra-Thoracic Airways. IEEE Trans. Medical Imaging 1997;16:820–827.
19. Reinhardt, JM.; Park, W.; Hoffman, EA.; Sonka, M. Intrathoracic airway wall detection using graph search with CT scanner PSF information; Proc. SPIE Conf. Medical Imaging, Newport Beach, CA. 23–28 Feb; 1997. p. 93-101.
20. Prêteux, F.; Fetita, CI.; Grenier, P. Statistical and Stochastic Methods in Image Processing II. 3167. San Diego, CA; 1997. Modeling, segmentation, and caliber estimation of bronchi in high-resolution computerized tomography; p. 58-69.SPIE Proceedings
21. Saba, OI.; Hoffman, EA.; Reinhardt, JM. Physiology and Function from Multidimensional Images. 3978. 2000. Computed Tomographic-Based Estimation of Airway Size with Correction for Scanned Plane Tilt Angle. Proc. of SPIE
22. Wiemker, R.; Blaffert, T.; Bülow, T.; Renisch, S.; Lorenz, C. CARS. 2004. Automated assessment of bronchial lumen, wall thickness and bronchoarterial diameter ratio of the tracheobronchial tree using high-resolution CT; p. 967-972.
23. Udupa JK, Samarasekera S. Fuzzy Connectedness and Object Definition: Theory, Algorithms, and Applications in Image Segmentation. Graphics Models and Image Processing 1996;58:246–261.
24. Herman GT, Carvalho BM. Multiseeded Segmentation Using Fuzzy Connectedness. Pattern Analysis and Machine Intelligence, IEEE Transactions on 2001;23:460–474.
25. Palágyi, K.; Tschirren, J.; Sonka, M. Quantitative analysis of three-dimensional tubular tree structures; SPIE Medical Imaging, San Diego, CA, USA. February 15.–20. 2003; 2003.

26. Sonka, M.; Hlavac, V.; Boyle, R. Image Processing, Analysis, and Machine Vision. Brooks/Cole Publishing Company; 1998.

27. Sonka M, Reddy GK, Winniford MD, Collins SM. Adaptive approach to accurate analysis of small-diameter vessels in cineangiograms. Medical Imaging, IEEE Transactions on 1997;16:87–95.

28. Kiraly AP, Higgins WE, McLennan G, Hoffman EA, Reinhardt JM. Three-dimensional Human Airway Segmentation Methods for Clinical Virtual Bronchoscopy. Academic Radiology 2002;9:1153–1168. [PubMed: 12385510]

29. Boyden, EA. Segmental anatomy of the lungs. McGraw-Hill; 1955.

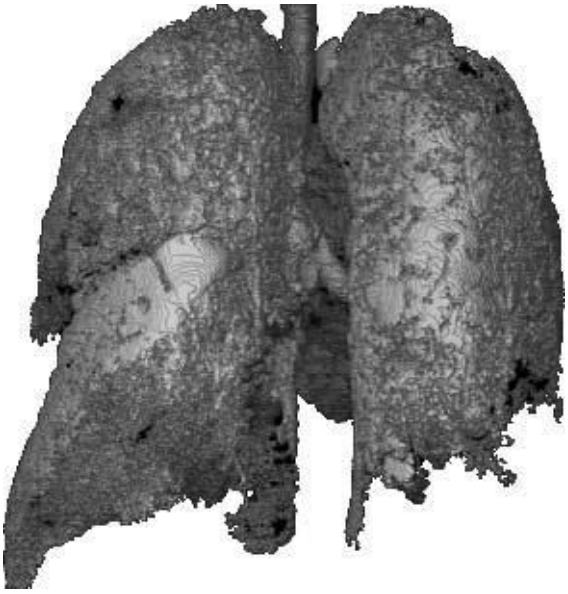

Fig. 1.
Example of a severe segmentation leak. (Emphysema patient, segmented with standard 3D region-grow algorithm — leak was unavoidable).

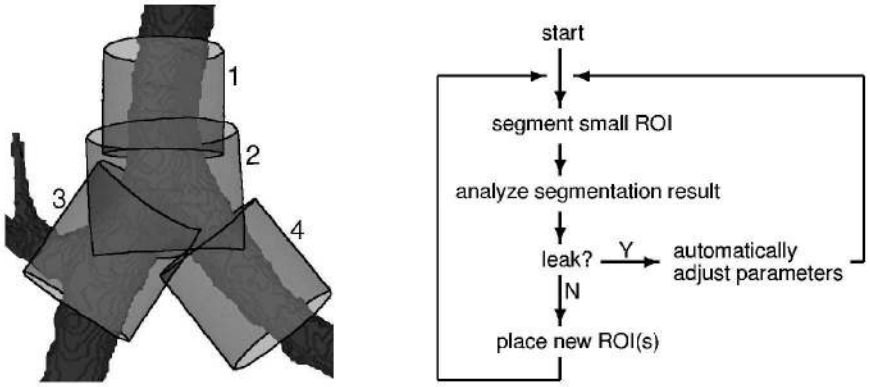

Fig. 2.

Basic concept of airway tree segmentation. Adaptive cylindrical regions of interest (light gray) follow airway tree branches as the segmentation proceeds. Segmentation is performed in a small area only, which keeps the computing time down. Possible problems (leaks) can be detected early and addressed. The simplified flow diagram to the right does not show all details (for example, the termination criteria).

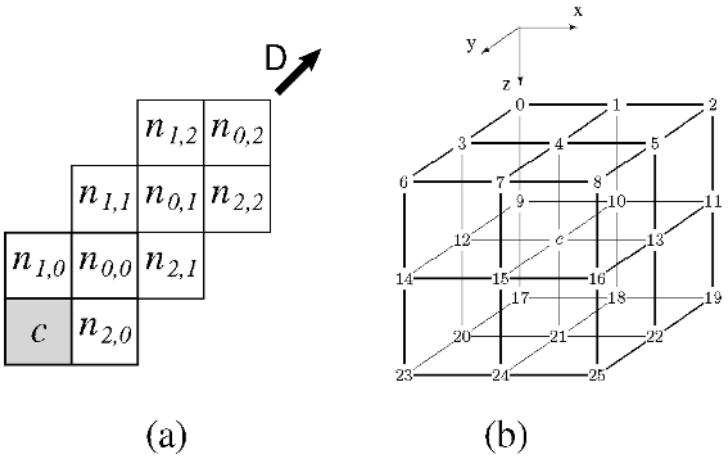

Fig. 3.

Directional affinity. a) Principle illustrated in 2D. Gray-values of $n_{*,1}$ and $n_{*,2}$ are included in computation of affinity between c and $n_{*,0}$. 'D' marks preferred direction. b) Possible values for 'D' in 3D.

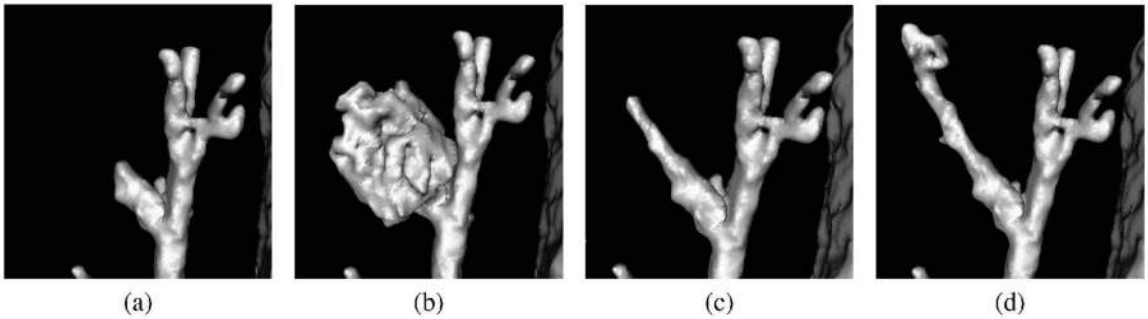

Fig. 4.
Example of result from directional affinity. a) New branch taking off to the left. b) A leak occurred and is detected. c) Previous step was deleted and by using directional affinity a new leak can be avoided. d) Segmentation of the branch continues with un-directed affinity function.

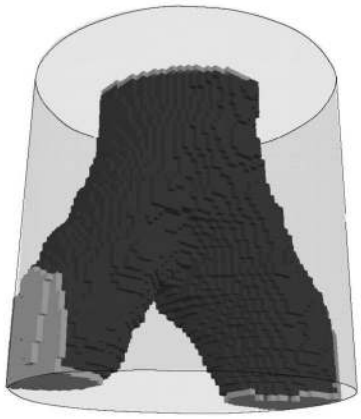

(a) Surface region growing result, with surface faces colored light gray.

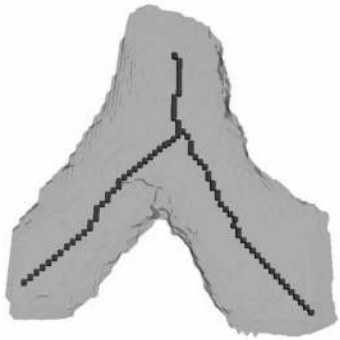

(b) Skeletonized segmentation result.

Fig. 5.

Analysis of segmentation result. (a) Surface region growing result, with surface faces colored light gray. (b) Skeletonized segmentation result.

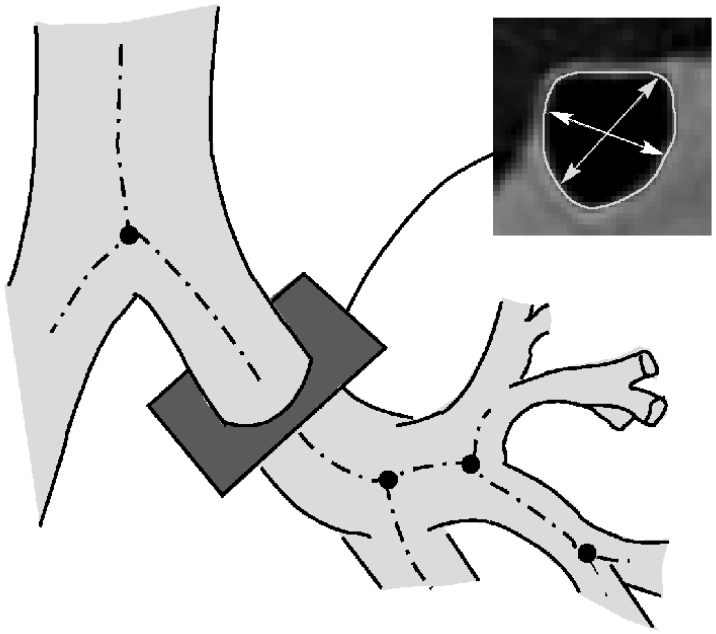

Fig. 6.
Quantitative analysis: 2D slices are re-sampled perpendicular to centerline, inner border is detected, cross-sectional area, minor-, and major-diameter are computed.

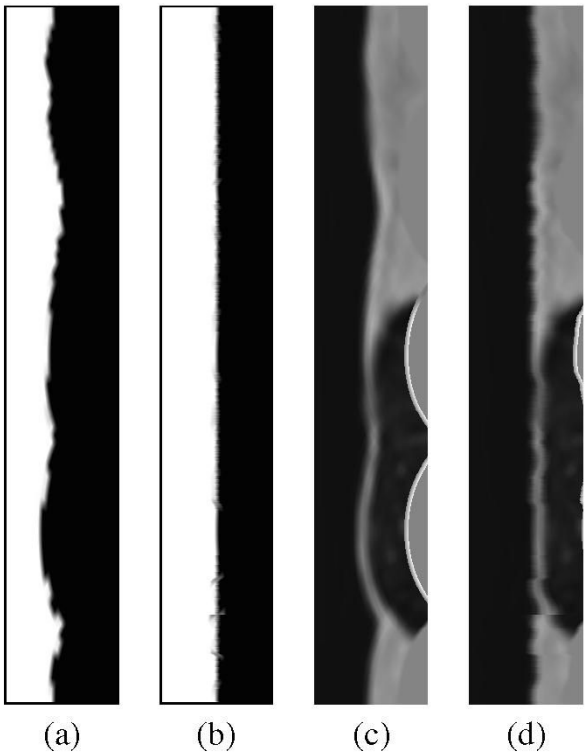

Fig. 7.
Radially re-sampled 2D cross-sections. a) Preliminary airway-segmentation result before shifting. b) Preliminary airway-segmentation result after shifting. c) Gray-level image before shifting. d) Gray-level image after shifting. The black frames around a) and b) have been added for visualization purposes only; they are not part of the original image.

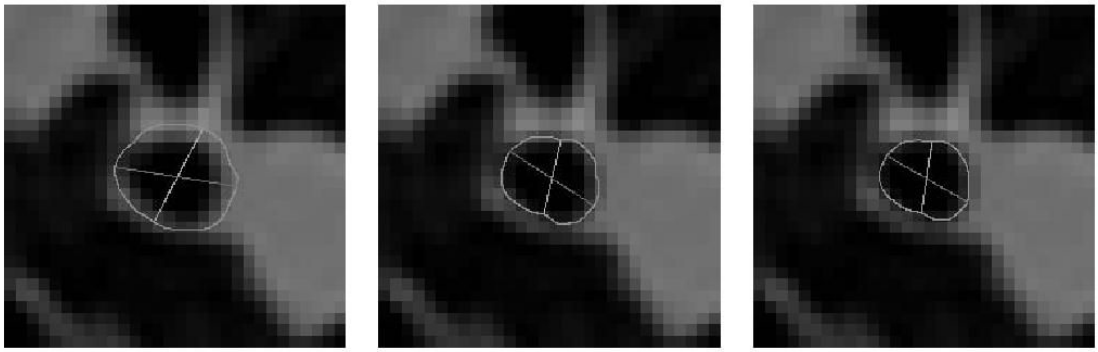

Fig. 8.
Border position can be modified by adjusting the value of ω in Equation 6. Note that the airway size is overestimated in a) and underestimated in c).

Fig. 9.
Piecewise linear function for ω in cost function. (Equation 6.) Estimated diameter is computed based on area from segmentation result (pixel-count in re-sampled slice).

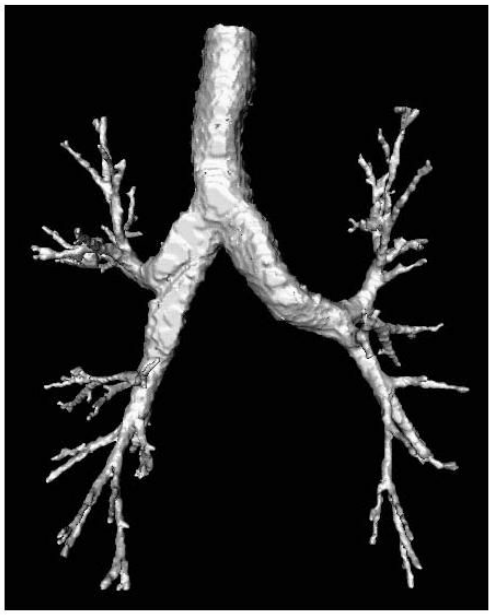

Fig. 10.
Segmentation result using the new method. Tree from the same CT scan as used in Figure 1.

Fig. 11.
Airway tree with assigned labels. Labels refer to segments, but are assigned to terminating branchpoint of respective segment. Drawing based on [29].

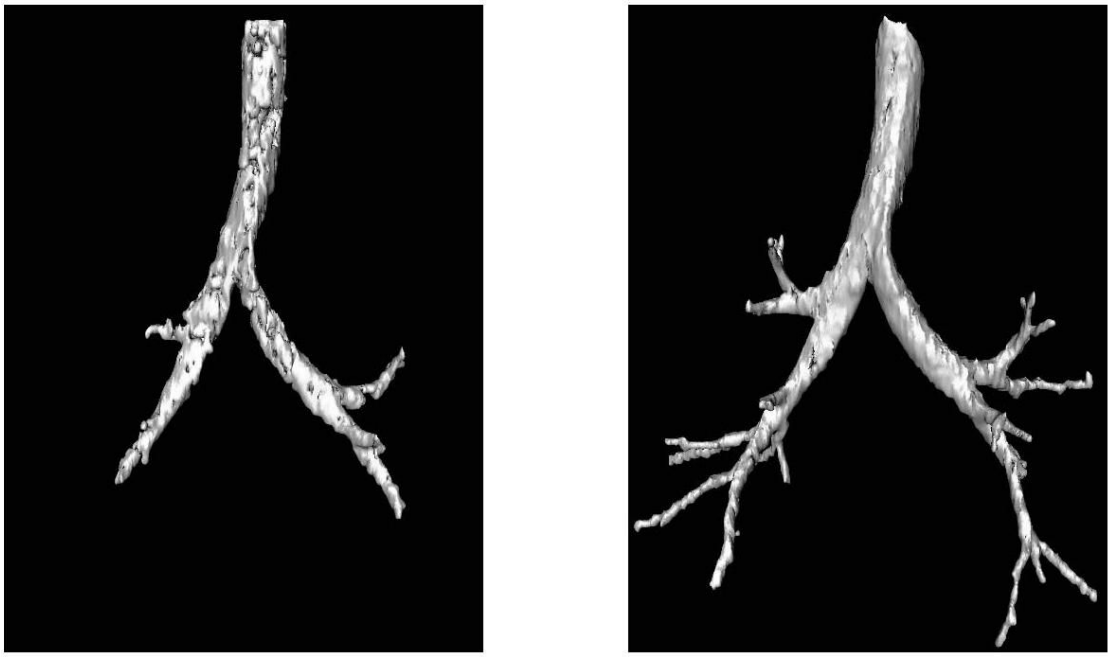

Fig. 12.
Segmentation result — low dose scan. (a) Region growing. Best possible result after hand-optimizing parameters. (b) Newly proposed algorithm. Fully automated run *without* changing parameters.

Fig. 13.
Diameters ± standard deviation of named segments. Based on 22 normal subjects.

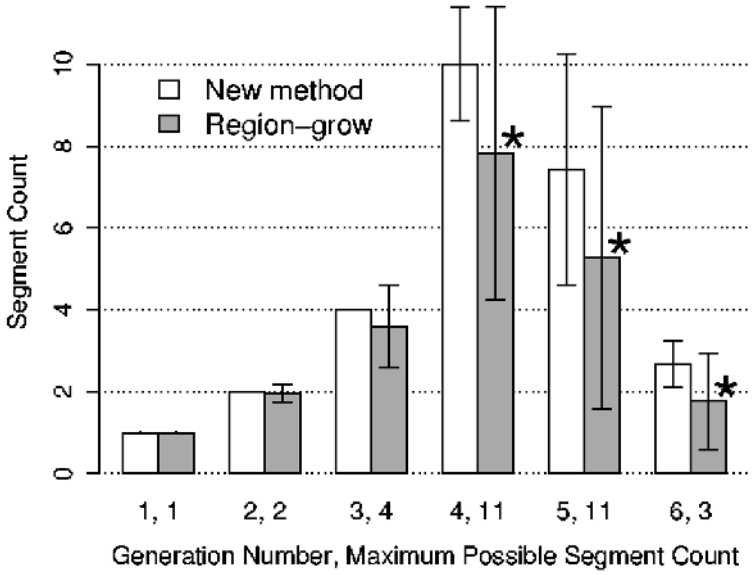

Fig. 14.

Count of retrieved anatomically named branches, sorted by generation number. Mean ± standard deviation are reported. For the generations marked with *, the new method retrieves a statistically significant higher count of branches ($p = 0.013$, 0.037, and 0.004 for generations 4, 5, and 6, respectively).

TABLE I

Comparison of number of successfully segmented named airway branches(column 2 and 3), and number of named airway branches not found by other segmentation method(column 4 and 5).

Subject	# of named segments		# of segments unique in	
	new method	region-grow	new method	region-grow
1	32	29	3	0
2	24	13	11	0
3	28	28	0	0
4	32	23	9	0
5	27	8	19	0
6	23	15	8	0
7	28	5	23	0
8	30	28	3	1
9	27	28	0	1
10	23	19	4	0
11	23	24	0	1
12	18	2	16	0
13	32	32	0	0
14	29	29	0	0
15	30	16	14	0
16	27	22	5	0
17	24	20	4	0
18	27	27	0	0
19	32	32	0	0
20	27	22	5	0
21	32	29	3	0
22	29	24	5	0
Overall Results Mean ± Stdev	27.45±3.75	21.59±8.59	6.00±6.73	0.14±0.35

TABLE II

Measurements on Plexiglas phantom. Low dose scan (120 kV, 50 mAs).

	Low dose							
	(d_{nom} - d_{μ}) [mm] for Tube *n*							
ψ	**1**	**2**	**3**	**4**	**5**	**6**	**μ**	**σ**
0°	-0.00	0.20	-0.03	-0.14	-0.16	0.04	-0.02	0.17
5°	0.11	0.07	-0.02	-0.12	-0.15	0.07	-0.01	0.14
30°	-0.07	-0.17	-0.12	-0.22	-0.26	-0.14	-0.16	0.09
90°	-0.31	0.01	-0.14	-0.12	-0.24	-0.22	-0.17	0.15
μ	-0.07	0.03	-0.08	-0.15	-0.20	-0.06		
σ	0.18	0.15	0.06	0.05	0.06	0.14		

TABLE III

Measurements on plexiglas phantom. Regular dose scan(120 kV, 100 mAs).

	Regular dose							
		(d_{nom} - d_{μ}) [mm] for Tube *n*						
ψ	**1**	**2**	**3**	**4**	**5**	**6**	**μ**	**σ**
0°	-0.00	0.20	-0.04	-0.16	-0.14	0.04	-0.02	0.17
5°	0.10	0.13	-0.02	-0.15	-0.15	0.06	-0.01	0.16
30°	-0.04	-0.12	-0.12	-0.22	-0.27	-0.17	-0.16	0.11
90°	-0.03	-0.01	0.01	-0.40	-0.46	-0.12	-0.17	0.27
μ	0.01	0.05	-0.04	-0.23	-0.25	-0.05		
σ	0.06	0.14	0.06	0.12	0.15	0.11		

TABLE IV

Measurements on Plexiglas phantom. High dose scan (120 kV,200 mAs).

	High dose							
	(d_{nom} - d_{μ}) [mm] for Tube *n*							
ψ	**1**	**2**	**3**	**4**	**5**	**6**	**μ**	**σ**
0°	-0.17	-0.19	-0.13	-0.19	-0.16	0.04	-0.13	0.11
5°	-0.17	-0.14	-0.15	-0.20	-0.15	0.05	-0.13	0.12
30°	-0.40	-0.19	-0.20	-0.31	-0.28	-0.17	-0.26	0.11
90°	-0.26	-0.11	-0.23	-0.33	-0.26	-0.13	-0.22	0.11
μ	-0.25	-0.16	-0.18	-0.26	-0.21	-0.05		
σ	0.11	0.04	0.05	0.07	0.07	0.11		